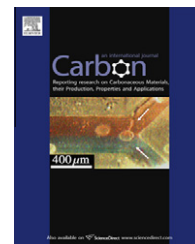


This article appeared in a journal published by Elsevier. The attached copy is furnished to the author for internal non-commercial research and education use, including for instruction at the authors institution and sharing with colleagues.

Other uses, including reproduction and distribution, or selling or licensing copies, or posting to personal, institutional or third party websites are prohibited.

In most cases authors are permitted to post their version of the article (e.g. in Word or Tex form) to their personal website or institutional repository. Authors requiring further information regarding Elsevier's archiving and manuscript policies are encouraged to visit:

<http://www.elsevier.com/copyright>

available at www.sciencedirect.comjournal homepage: www.elsevier.com/locate/carbon

Carbon nanotube toughened hydroxyapatite by spark plasma sintering: Microstructural evolution and multiscale tribological properties

Debrupa Lahiri ^a, Virendra Singh ^b, Anup K. Keshri ^a, Sudipta Seal ^b, Arvind Agarwal ^{a,*}

^a Plasma Forming Laboratory and Nanomechanics and Nanotribology Laboratory, Mechanical and Materials Engineering, 10555 West Flagler Street, EC 3464, Florida International University, Miami, FL 33174, USA

^b AMPAC and Nanoscience Technology Center, 4000 Central FL Blvd, AMPAC, Eng 1 Room 381, University of Central Florida, Orlando 32816, USA

ARTICLE INFO

Article history:

Received 8 January 2010

Accepted 23 April 2010

Available online 23 May 2010

ABSTRACT

Carbon nanotube (CNT) reinforced hydroxyapatite (HA) composite synthesized using spark plasma sintering is investigated in this study. Quantitative microstructural analysis suggests that CNTs play a role in grain boundary pinning and are responsible for the improved densification and retention of nanostructure throughout the thickness of the sintered pellet. HA crystal forms coherent interface with the CNT, resulting in a strong interfacial bond. The uniform distribution of 4 wt.% CNTs in the HA matrix, good interfacial bonding and fine HA grain size help to improve the fracture toughness by 92% and elastic modulus by 25% as compared to the HA matrix without CNT. Toughening mechanisms have been explained in terms of interfacial shear strength and pull-out energy of CNT from the HA matrix. CNT plays a major role in improving the wear resistance of HA matrix at both macro- and nano-scale. It is concluded that graphene layer removal from the CNT surface occurs during macro-wear, but not for nano-wear. Thus, the coefficient of friction (CoF) in HA–CNT decreases in macro-wear due to lubrication available through delaminated graphene layers.

© 2010 Elsevier Ltd. All rights reserved.

1. Introduction

Hydroxyapatite (HA) is an attractive material for bone substitution and reconstruction owing to its chemical composition ($\text{Ca}_{10}(\text{PO}_4)_6(\text{OH})_2$), crystal structure and calcium to phosphate ratio (1.67), which is very similar to that of apatite found in the human skeletal system [1–3]. Because of its unique bioactive and osteoconductive properties, HA has been clinically tested and accepted for orthopedic applications. However limited stability of HA causes its dissociation into tricalcium phosphate (TCP) and tetracalcium phosphate, during prolonged exposure at high temperature processing [1,4]. Further, the mechanical properties of HA are insufficient for

major load bearing implants. The fracture toughness of dense HA ($1 \text{ MPa m}^{0.5}$) is just half of the minimum reported fracture toughness of cortical bone ($2\text{--}12 \text{ MPa m}^{0.5}$) [3]. Poor wear resistance of HA is another drawback for its successful application in orthopedic implants [2,3,5–7].

Nanocrystalline HA has been utilized by several researchers [8–12] to overcome some of these limitations. The development of nanoparticles has been accompanied by the need for a suitable processing technique to retain the fine grain size. Spark plasma sintering (SPS) has proved to be a promising technique for the sintering of nanoceramics [13–17]. Due to simultaneous application of pressure, electrical current, and rapid heating rate, SPS offers better densification of

* Corresponding author. Fax: +1 305 348 1932.

E-mail address: agarwala@fiu.edu (A. Agarwal).

0008-6223/\$ - see front matter © 2010 Elsevier Ltd. All rights reserved.

doi:10.1016/j.carbon.2010.04.047

nanoceramic particles at a temperature lower than that of conventional sintering. At the same time, due to a shorter sintering time, SPS retains the nanostructure and thus, results in improved mechanical properties of the sintered body [15–19]. Studies on the processing of HA by SPS have shown better densification as well as less dissociation into TCP [1,2,5,8,20,21]. Moreover, SPS processed HA surface has shown better osteoblast cell proliferation than conventionally sintered HA surface, proving SPS HA to be a better candidate for the clinical application [8,9].

The low fracture toughness and poor wear resistance of HA can be improved by adding second phase reinforcement. Carbon nanotube (CNT) has already shown its potential as an effective reinforcement for HA and other ceramics [22–25] to improve the fracture toughness. Reports are available on the processing of HA–CNT composite coating for orthopedic implants through plasma spraying [6,26–28], laser surface alloying [7,29], electrophoretic deposition [30,31], and aerosol deposition [32]. In addition to the conventional sintering [33,34] and hot isostatic pressing [35,36], SPS [37–39] has also been employed for the fabrication of free standing HA–CNT composite. Omori et al. [37] have reported consolidation of multiwall carbon nanotubes by SPS and then dip-coating with HA, followed by a second round of SPS consolidation of the coated preform. They observed a consolidated coating of HA on CNT without any crack formation. One of the other two studies on SPS of HA–CNT composite has used nano-HA powders and CNTs, mixed by ball milling, as the starting material [38]. Sarkar et al. have found the fracture toughness of HA–CNT composite to be as high as $1.27 \text{ MPa m}^{0.5}$ with 2.5 vol.% CNT addition, which was 30% increase over HA [38]. Xu et al. have performed extensive mechanical stirring to homogeneously mix the CNTs with spray-dried HA powder to prepare the feedstock for SPS processing [39]. Young's modulus has been reported to be 131 GPa with 2 vol.% CNT addition, though no direct comparison with HA has been presented [39]. The biocompatibility of CNT reinforced HA composite has also been studied by Xu et al. and concluded the beneficial effect of CNT on the osteoblast cell proliferation [39]. However, none of these reports provides insight on the effects of CNT in altering the densification mechanism, grain structure and morphology of HA–CNT composite during SPS processing. Role of CNT in improving the mechanical property of SPS processed HA-based composite also owes a detailed investigation and explanation. Moreover, to the best of author's knowledge, there is no study on tribological properties of SPS processed HA–CNT composites, which is important for orthopedic applications.

Hence one of the aims of this study is to investigate the role of CNT in the microstructural evolution of HA-based composite during SPS process. This has been carried out by studying the grain size, and porosity and correlating with the physical properties of CNT such as thermal and electrical conductivity. The effect of CNT modified microstructure and HA/CNT interface on Young's modulus and fracture toughness of the composite is also elucidated. Macro- and nano-scale tribological properties of SPS HA–CNT composite have

been studied in terms of wear resistance and coefficient of friction. The differential roles played by CNT in tribological properties, over multiple length scales have been addressed. This study does not perform any biocompatibility related experiments, because the biocompatibility for the same composition (HA–4 wt.% CNT) has already been proven in terms of osteoblast cell growth by Balani et al. [26]. In another study for a similar composite and processing route, Xu et al. have also claimed, that presence of CNT is beneficial for osteoblast cell growth [39]. We also acknowledge the ongoing debate about the biocompatibility of CNTs [40–43], but it is not the focus of this study.

2. Materials and methods

2.1. Materials

HA-nanorods (length: 100–325 nm, diameter: 25–50 nm, density: 3.2 g cm^{-3}) and multiwall carbon nanotubes (95% purity, 40–70 nm outer diameter, 1–3 μm in length, density: 2.1 g cm^{-3}), procured from Inframat Corporation (Wilmington, CT, USA), were used as the precursor powder as shown in Fig 1a and b, respectively. HA-nanorods and CNTs were spray-dried together to synthesize the composite agglomerates with a size of 15–55 μm (Fig. 1c). During spray-drying, HA-nanorods and CNTs were dispersed together, in a water soluble organic binder. The suspension was sprayed in an atomized chamber and dried subsequently, to obtain micron size porous spherical agglomerates. Spray-dried powders were made by Inframat Corporation. Spray-dried powder enables a higher degree of homogeneity of CNT distribution in the HA matrix [44]. It is emphasized that none of the earlier studies on HA–CNT utilized spray-dried composite powder [38,39].

2.2. Spark plasma sintering

Consolidation of spray-dried HA and HA–CNT powders was performed using the spark plasma sintering facility at Thermal Technology LLC, Sana Rosa, California, USA. The SPS was carried out at 60 MPa pressure and 1373 K in vacuum using the graphite die. A rapid heating rate of 360 K/min with a hold time of 5 min at the highest temperature was used. Pellets of 19.5 mm diameter and $\sim 5 \text{ mm}$ thickness were consolidated. The compositions used in this study are 100% HA and HA–4 wt.% CNT, which will be referred as HA and HA–CNT, respectively.

2.3. Microstructural characterization

Sintered pellets were polished to remove the graphitic contamination on the surface. The samples were sectioned, mounted and metallographically polished for the microstructure characterization. A FEI PHENOM scanning electron microscope and a JEOL JSM-6330F field emission scanning electron microscope, operating at 5 kV and 15 kV, respectively, were used for the characterization of powders and SPS pellets. ImageJ¹ software was used for the quantitative analysis

¹ Rasband WS, ImageJ, US National Institutes of Health, Bethesda, Maryland, USA, <http://rsb.info.nih.gov/ij/>, 1997–2009.

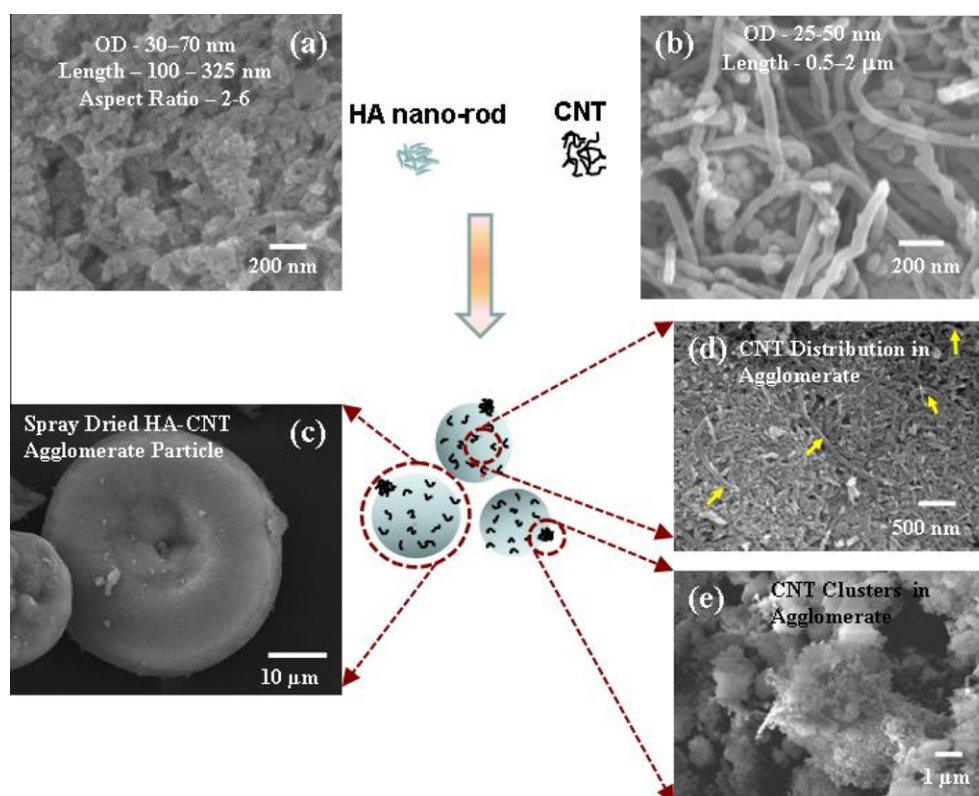


Fig. 1 – Schematic of formation of spray-dried HA–CNT composite powder from HA-nanorods and CNTs and SEM micrographs of (a) HA-nanorods, (b) multiwalled CNTs, (c) spray-dried HA–CNT agglomerate, (d) distribution of CNT in spray-dried HA–CNT and (e) some CNT clusters on HA–CNT agglomerate surface.

of microstructural features. Philips/FEI Tecnai F30 high resolution transmission electron microscope (HRTEM) operating at an accelerating voltage of 300 kV was used to study CNTs and HA/CNT interface after spark plasma sintering. Forward and inverse Fourier transform (FFT and Inverse-FFT) analysis has been used for the accurate calculation of the lattice spacing. Density has been measured using Archimedes principle and water as the immersing medium.

X-ray diffraction (XRD) study on the spray-dried powders and sintered pellets was carried out using Cu K α ($\lambda = 1.542 \text{ \AA}$) radiation in a Siemens D5000 X-ray diffractometer operating at 40 kV and 40 mA. A scan rate of $0.2^\circ/\text{min}$ and a step size of 0.01° have been used to obtain XRD profiles. Micro-Raman spectroscopy of the spray-dried powder, sintered pellet and wear track was performed using a Spectra Physics (Model 3900S, California, USA) with Ti-sapphire crystal as target, a laser power of 18 mW and the detector from Kaiser Optical Systems, Inc. (Michigan, USA).

2.4. Mechanical and tribological characterization

Hysitron Triboindenter (Hysitron Inc., Minneapolis, MN, USA) with 100 nm Berkovich pyramidal tip, was used in quasi-static indentation mode to measure the elastic modulus and hardness of the sintered pellets. Tip-area calibration was done using a standard fused quartz substrate of known modulus

(69.6 GPa). Indentation was performed with a constant loading/unloading rate for 10 s and 3 s hold at the peak load of $2500 \mu\text{N}$. Elastic modulus (E) had been calculated from the load–displacement curves using Oliver–Pharr method [45]. For nano-wear study, triboindenter was used in 2D scratch mode. The scratches of $10 \mu\text{m}$ length were made with constant normal loads of $3500 \mu\text{N}$ and $4500 \mu\text{N}$. Lateral force and scratch depth along the scratch length was recorded by two different piezoelectric sensors working in directions perpendicular to each other. Scratch profiles were obtained by the scanning probe microscopy (SPM) with the same tip at a set-point load of $2 \mu\text{N}$. The topography image processing was performed using SPIP² version 4.5.1 (Image Metrology, Denmark). Scratch volume calculation has been performed from the geometry of the scratches obtained through 2D profiles of scratch along the length and width, which is explained in Section 3.4.2 of this study. The methodology of wear volume calculations in a nano-scratch study is based on the method suggested by Bakshi et al. [46]. Both, the nanoindentation and nano-scratch study have been performed on the metallographically polished cross-section of the sintered pellets.

Microhardness was measured using a microhardness tester (Shanghai Taiming Optical Instrument Co. Ltd., model HXD-1000 TMC, Shanghai) with a Vickers probe and application of 1 kg load for 15 s of dwell time. For an accurate

² SPIP: Image Processing Software for Microscopy, version 4.5.1, Image Metrology, DK-2970 Hørsholm, Denmark.

measurement of radial crack length, the indents were observed under SEM.

Ball-on disk tribometer (Nanovea, Micro Photonics Inc., CA) was used to evaluate the macro-scale wear resistance and coefficient of friction (CoF) of the sintered pellets. Surface of sintered HA and HA–CNT pellets was polished to a roughness (R_a) of 0.5 μm or less. Macro-wear studies were performed at 50 rpm speed with a circular track of 2 mm radius and a total travel distance of 100 m. An alumina ball of 3 mm diameter was used as the counter surface. The lateral force between the alumina ball and the sintered pellet surface and depth of wear track has been measured by the linear variable differential transformer (LVDT) sensor. The coefficient of friction data was acquired at a frequency of 16.67 Hz.

3. Results and discussion

3.1. Microstructural evolution

HA–CNT composite powder, synthesized through spray-drying process, shows bimodal distribution of CNT. Nanotubes were found nicely dispersed inside the porous spray-dried agglomerate, whereas, loose CNT clusters were also present on the surface (Fig. 1d and e). Spark plasma sintered HA and HA–CNT pellets showed density value of 94.9 (± 0.57) and 96.5 (± 0.49)% TD, respectively. The density values reveals slightly better densification in HA–CNT.

Fig. 2 presents the fracture surface of sintered HA and HA–CNT pellets at different magnifications. The microstructure reveals two prominent regions present in both HA and HA–CNT. They are (i) larger, fully densified monolithic regions and (ii) small grain regions (Fig. 2a and b). Apart from these two features, porosity is also present in HA fracture surface (Figs. 2c and 3a). HA–CNT structure does not show porosity. The distribution of CNT in the sintered HA–CNT pellet is directly related to their distribution in the powder stage. Uniformly distributed CNTs are found in both fine grained and monolithic regions (Fig. 2d and e), whereas CNT clusters are largely found in and around fine grained region (Fig. 2f). It is also observed that distribution and morphology of monolithic region, fine grain regions and pores vary from the periphery to the centre of the pellets for both compositions. Table 1 summarizes the microstructural variations in the quantitative terms. The values presented in Table 1 are based on the area fraction of microstructural features in the micrographs. All these features are attributed to SPS processing in conjunction with the presence of CNTs. A detailed explanation of the microstructure evolution is discussed below in terms of three main features, viz. (i) monolithic region, (ii) fine grained region and (iii) porosity in HA or HA/CNT clusters.

3.1.1. Monolithic region

The monolithic region forms due to rapid grain growth, which is also known as dynamic ripening [47]. The heating rate used in this study is 360 K/min. The rapid heating rate is achieved through application of high current density that causes localized joule heating at particle interfaces. Such localized heating helps in accelerated thermal diffusion, melting within inter-particle contact areas and also creates

thermal stresses which enable dislocation creep. Thus, spark plasma sintering by-passes the initial stage of surface diffusion, as in conventional sintering, and achieves accelerated densification by early activation of diffusion mechanisms, like grain boundary and lattice diffusion and power-law dislocation creep [17–19], leading to formation of consolidated monolithic regions.

But, HA is a ceramic with poor thermal conductivity (1.25 W/mK [48]). As the heating source is the graphite die in contact with the periphery of the green pellet, a thermal gradient is created along the pellet thickness with the lowest temperature at the centre. This non-uniform temperature distribution promotes a densification gradient along the pellet thickness (~ 5 mm) resulting into microstructural variation. Poor electrical conductivity of HA ($7 \times 10^{-7} \text{ S cm}^{-1}$) [49], adds to the density gradient throughout the pellet thickness. Joule heating and electrical field assisted mass transport decreases towards the centre of the pellet due to existing electrical field gradient across the thickness. As a result, HA pellet goes through more densification at the periphery than in centre. Such differential densification leads to more monolithic regions at the periphery (48%) as compared to the centre (35%) in the sintered structure (Table 1).

On the contrary, thermal conductivity of CNT (2980 W/mK) [50] is three orders of magnitude higher than HA (1.25 W/mK), which results into higher effective thermal conductivity of the HA–CNT composite powder. Similarly, higher electrical conductivity of CNT ($2 \times 10^4 \text{ S cm}^{-1}$) [51] than HA ($7 \times 10^{-7} \text{ S cm}^{-1}$), increases the effective electrical conductivity of HA–CNT composite and reduces the electrical field gradient across the green HA–CNT pellet. The reduction in both, thermal and electrical gradient results in reducing the densification gradient along the thickness of HA–CNT pellet. Thus, in case of HA–CNT pellet, only 3% difference in monolithic content is observed from the periphery (21%) to the centre (18%) as presented in Table 1. The increase in effective thermal and electrical conductivity of HA–CNT also helps in overall better densification than HA, as evident from the measured density of 96.5% and 94.9% TD, respectively. The application of pressure in SPS also helps in densification by increasing particle surface contact through particle rearrangement, breaking of CNT agglomerates and thus promoting easy diffusion at lower temperature, which is absent in conventional sintering. Effect of thermal, electrical and pressure gradient on the microstructure evolution during SPS of HA and HA–CNT has been explained through a schematic diagram in Fig. 4.

3.1.2. Fine grained region

Fine grain regions are observed in both HA and HA–CNT pellets. But, the origin of fine grain region is different in HA and HA–CNT, which is evident from Fig. 2a–d. Fine grain regions in SPS-HA pellet is generated due to incomplete sintering or less densification. SEM micrograph of fine grain region in HA shows presence of porosity and partially sintered structure (Fig. 2c). Due to less densification at the centre, fraction of fine grain region is also higher at the centre (55%) than in periphery (47%) in HA pellet (Table 1). HA–CNT pellet contains higher fraction ($\sim 70\%$) of fine grained region than HA pellet as shown in Fig. 2b. The fine grain structure in HA–CNT is the

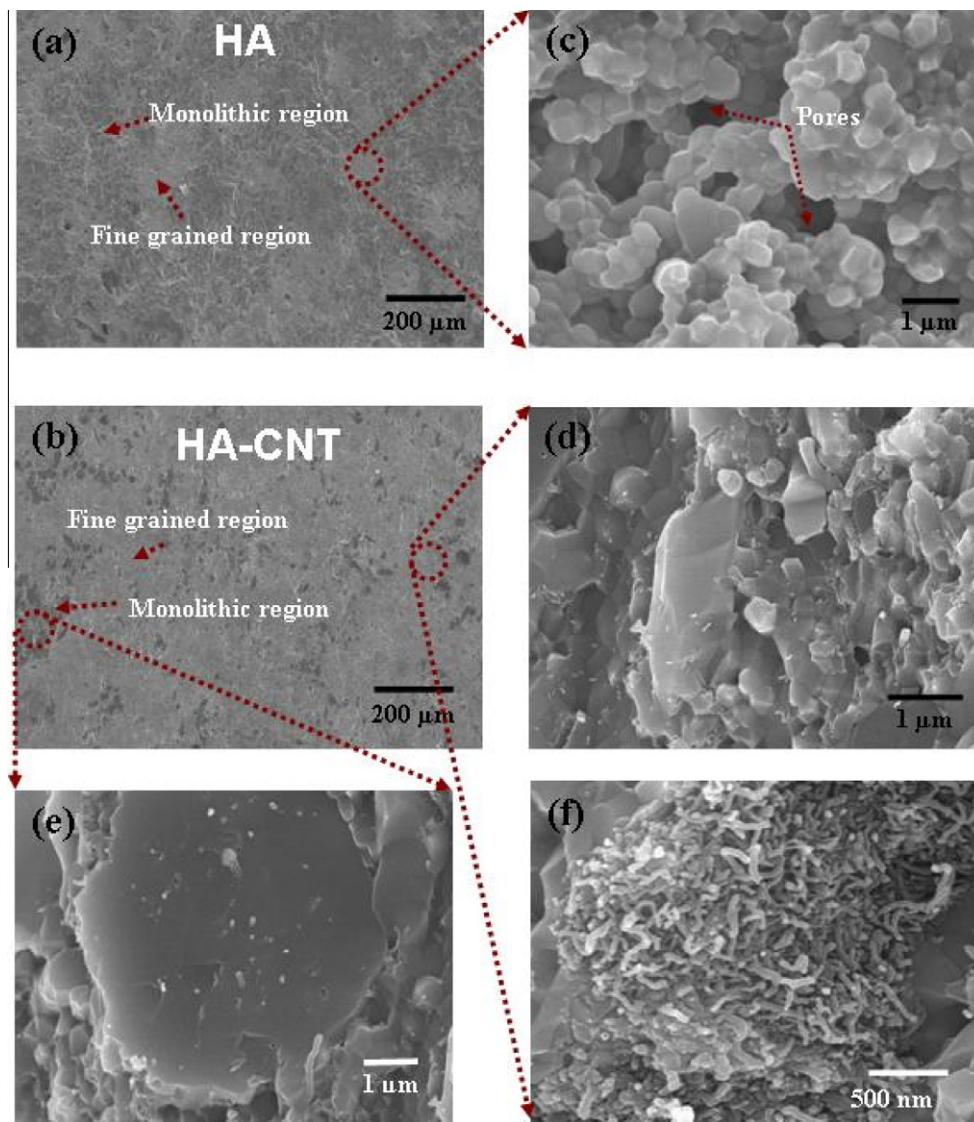


Fig. 2 – SEM micrographs of fracture surface of SPS pellets showing: (a) monolithic and fine grain region in HA, (b) monolithic and fine grain region in HA–CNT, (c) partially sintered HA structure with fine grain region and porosity, (d) fully densified fine grain region of HA–CNT with homogeneously distributed CNTs, (e) monolithic region of HA–CNT with CNTs embedded in HA matrix and (f) CNT clusters at fine grain region of HA–CNT.

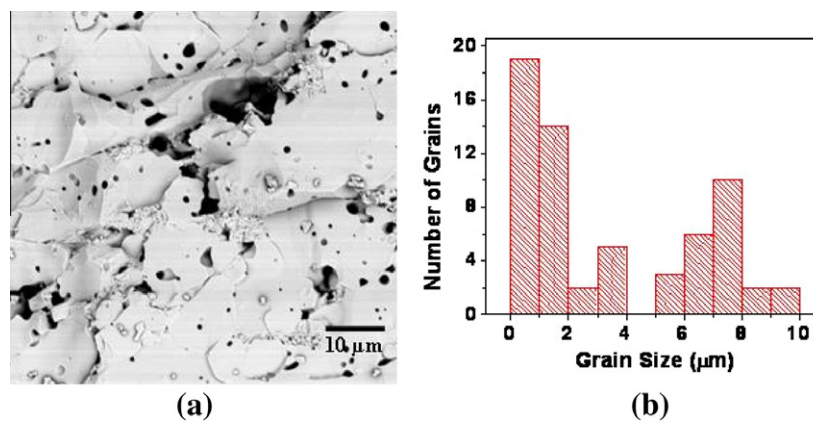
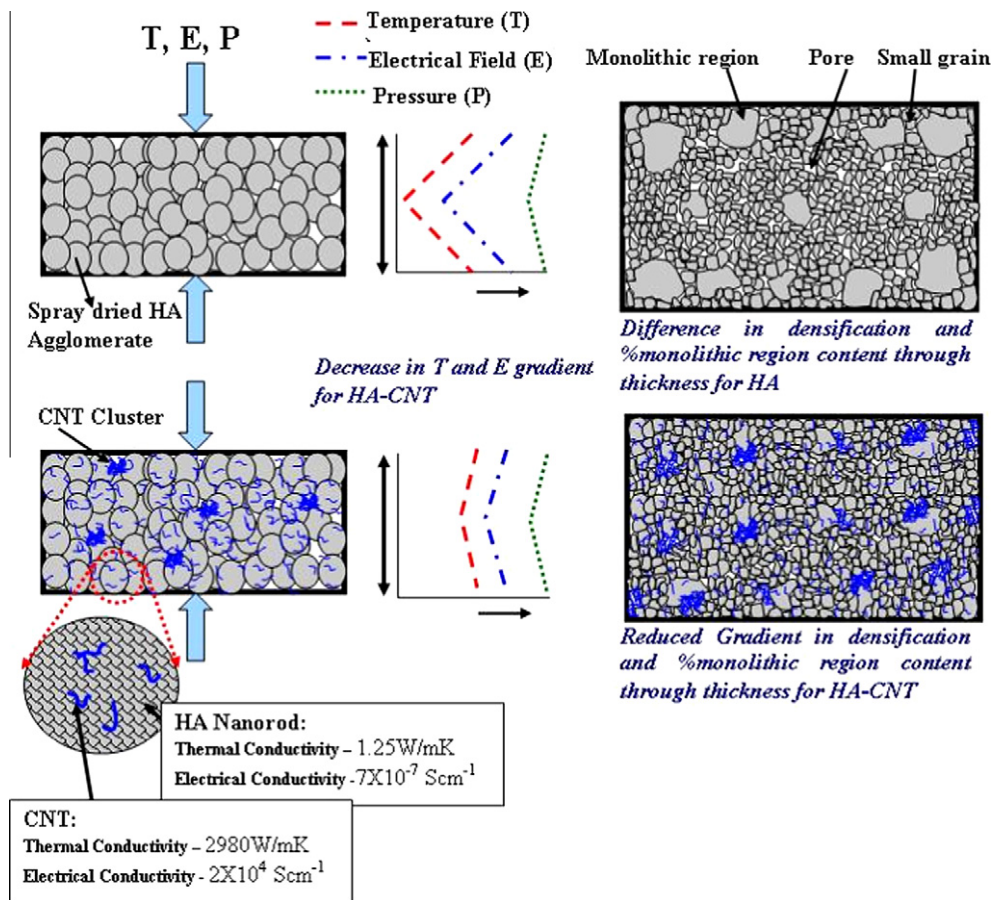


Fig. 3 – (a) SEM micrograph of fracture surface of SPS-HA pellet showing porosity and (b) histogram showing bimodal porosity distribution in SPS-HA pellet.

Table 1 – Comparative quantification of microstructural features in spark plasma sintered HA and HA–CNT pellets.

Microstructural features	HA-pellet		HA–CNT-pellet	
	Periphery	Centre	Periphery	Centre
Monolithic region size (μm)	207 ± 50	179 ± 41	15 ± 6	14 ± 6
Small grain size (μm)	0.6 ± 0.2	0.5 ± 0.1	0.4 ± 0.1	0.6 ± 0.1
% Monolithic region	48 ± 3	35 ± 2	21 ± 3	18 ± 3
% Porosity	5 ± 1	10 ± 1.5	5 ± 1.8^a	5 ± 2.5^a
% Small grain region	47 ± 2	55 ± 2	74 ± 2	77 ± 3

Values presented in the table are based on % area measurement from the micrographs.
^a Indicates CNT clusters (no visible pores are observed in HA–CNT).

**Fig. 4 – Schematic showing effect of SPS and CNT on the consolidation mechanism and microstructural evolution in HA and HA–CNT pellets.**

result of grain boundary pinning of HA by CNTs. The grain growth is controlled by the random dispersion of rigid immobile spherical second phase particle through grain boundary pinning and the maximum attainable grain size R can be expressed as,

$$R = a \frac{r}{f^b} \quad (1)$$

where r is the radius of the second phase particle, f is the volume fraction of the second phase particle and a , b are constants [52]. The Zener pinning factor Z is defined as,

$$Z = \frac{f}{r} \quad (2)$$

Sun et al. have modified expression of Z to get rid of the assumption about second phase particle shape and size [53]. According to their findings,

$$Z = \frac{S_v}{4} \quad (3)$$

S_v is defined as the surface area of particle per unit volume. S_v is very high for CNTs due to their large surface to volume ratio. As the S_v increases, R decreases, which means CNTs have a great potential of grain size refinement. Pinning at the grain boundary also retards the dynamic ripening process resulting in smaller size of monolithic regions. Thus, HA–CNT structure contains higher fraction of fine grained region as well as

smaller size of monolithic regions ($\sim 15 \mu\text{m}$) than HA ($\sim 200 \mu\text{m}$). Presence of CNT at the HA grain boundary in fine grain region of HA–CNT fracture surface (Fig. 2d) provides the visual evidence of grain boundary pinning by nanotubes. The fraction of fine grain region in HA–CNT remains same in the centre ($\sim 77\%$) and periphery region ($\sim 74\%$), as presented in Table 1. This uniformity could be attributed to the uniform distribution of CNT in the pellet, which controls the formation of fine grain region in HA–CNT.

3.1.3. Porosity

Porosity present in HA shows a bimodal distribution (Fig. 3a and b). The big pores are generated from the inter-particle gap, which are more pronounced at the centre of the doughnut shaped spray-dried agglomerates (Fig. 1c). The small pores originate from the regions of agglomerates having loosely bound HA particles. Due to poor thermal and electrical conductivity of HA, the inter-particle distances could not be covered fully during diffusion/densification. Presence of a sharp porosity gradient through thickness, with higher porosity in the centre (10%) than periphery (5%) (Table 1) is the result of densification gradient. Increase in the porosity content due to presence of thermal gradient in SPS of ceramic has also been observed by other researchers [54]. HA–CNT composite fracture surface shows presence of some CNT clusters and absence of porosity (Fig. 2b). The absence of porosity is already justified in terms of better densification achieved due to better thermal and electrical conductivity of CNT. The dense CNT clusters prevent the penetration of HA particles between them due to the short sintering period restricting long distance mass transport. The content of CNT cluster is the same for periphery (5%) and centre (5%) of the sintered pellet.

3.2. Structural evolution

X-ray diffraction patterns of HA and HA–CNT at both stages, viz. powder and after SPS consolidation are presented in Fig. 5. The major peaks in all four patterns are from hydroxyapatite (JCPDS PDF No. 9-432). Low intensity graphite peaks are observed in HA–CNT powder and SPS pellet. The graphite

peaks look weak because of the presence of strong HA peaks in the vicinity. The 100% peak of β -TCP (at $2\theta = 30.9^\circ$) and the third highest intensity peak ($2\theta = 27.67^\circ$) are absent in the XRD plots after SPS. The second highest intensity peak of TCP ($2\theta = 34.18^\circ$) overlaps with another peak of HA ($2\theta = 34.01^\circ$). Similarly, the highest peak of α -TCP ($2\theta = 30.69^\circ$) is also absent and the second highest peak ($2\theta = 22.88^\circ$) overlaps with a HA peak ($2\theta = 22.77^\circ$). Hence, the presence of α -TCP (JCPDS PDF No. 29-359) or β -TCP phase (JCPDS PDF No. 9-169) cannot be concluded. These observations prove that HA does not dissociate into TCP during SPS processing for both compositions. Previous studies on SPS HA–CNT composites report partial decomposition of HA into TCP [38,39]. But, the heating rate used in those studies (100 K/min) is 3.6 times lower than the heating rate in this study (360 K/min). The faster heating rate has reduced the total time of sintering, thus preventing the dissociation of HA into TCP. Since TCP was not found in the sintered pellets, further investigation on presence of CaO or tetra-CP was not carried out.

The HA peaks were more sharp after SPS processing, which indicates increase in the crystallinity of HA through accelerated grain boundary and lattice diffusion. In the HA–CNT composite, the relative height of the first and second highest intensity peaks gets reversed after SPS. The intensity of (0 0 2) peak in the powder ($2\theta = 25.87^\circ$) reduces in the sintered pellet whereas intensity of (2 1 0) peak in the powder ($2\theta = 28.95^\circ$) increases significantly after sintering. A plausible explanation for such behavior is the evolution of preferred crystallographic orientation in HA and HA–CNT due to high temperature exposure [55–57].

Raman spectrum of HA–CNT powder and sintered pellet shows the presence of G and D peaks of CNT (Fig. 6a), which are characteristics of sp^2 and sp^3 bonds of hexagonal carbon structure [58]. The peak at the lower wave number ($950\text{--}960 \text{ cm}^{-1}$) is from the ν_1 symmetric stretching vibration of phosphate anions in HA [59]. The appearance of G peaks at around 1580 cm^{-1} is the signature of highly pure graphitic structure whereas D peak (at around 1350 cm^{-1}) originates from a disorder-induced mode in the graphite. The intensity ratio of D and G peaks (I_D/I_G) is the index of defect density present in CNT. Fig. 6a shows an increase in I_D/I_G from the

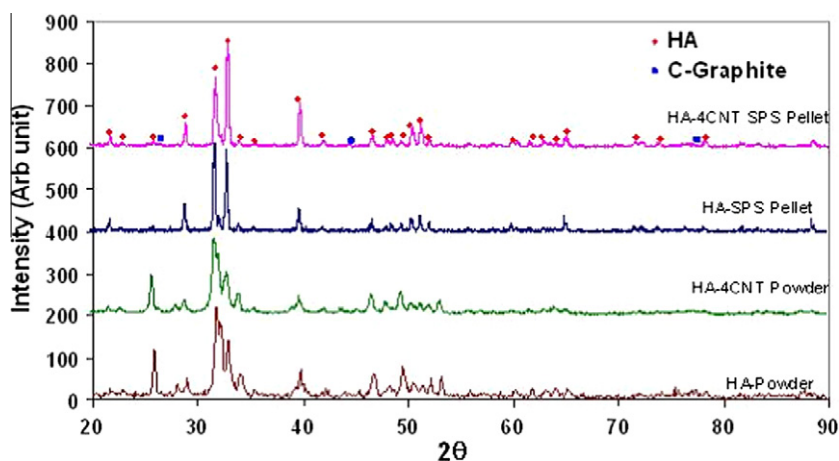


Fig. 5 – X-ray diffraction patterns of spray-dried HA and HA–CNT powders and SPS pellets.

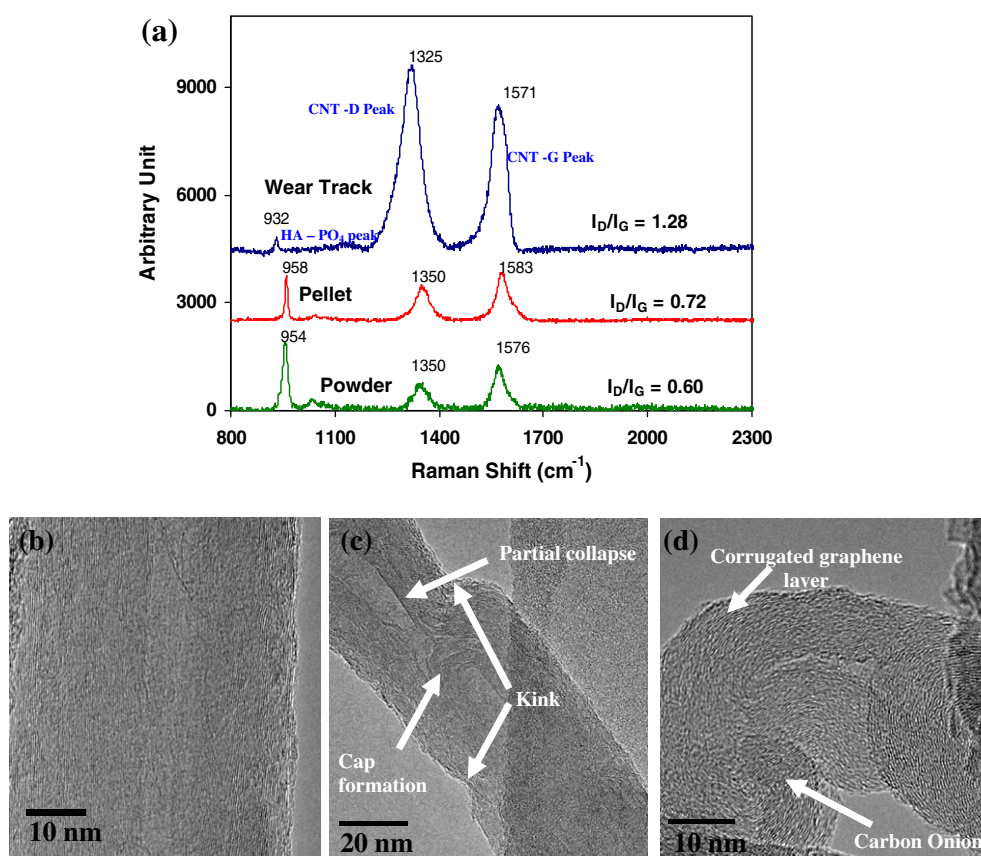


Fig. 6 – (a) Raman spectrum for HA–CNT powder, SPS pellet and wear track on SPS pellet showing D and G peak of CNT and phosphate peak of HA. (b) HRTEM of as-received defect-free CNT (c and d) HRTEM images of CNT in SPS HA–CNT pellet showing defects induced in CNT.

powder stage to the SPS HA–CNT composite. This observation indicates increase in the defect density in CNT as a result of SPS processing. A shift in the G band towards higher wave number has also been observed after SPS. This observation concurs with Das et al. on shift of the G peak to higher wave number with an increase in the defect density in graphite [60]. Absence of shift in D peak and the phosphate peak (HA) rules out the possibility of presence of compressive stress in the composite.

Fig. 6b shows a HRTEM image of as-received CNT which is largely defect-free. The defect induced in CNTs during SPS processing are observed in Fig. 6c and d. Disturbed arrangement of concentric tubular walls in CNTs with presence of different types of defects, e.g. carbon onion, cap formation, kink, partial collapse of nanotube walls and corrugated structure of graphene layers are observed in Fig. 6c and d. All these features are results of high temperature, pressure and current density applied in SPS processing. Kink and cap formation, and partial or full collapse of CNT walls upon application of high pressure has also been observed in cold spraying and SPS [61,62].

3.3. Carbon nanotube/hydroxyapatite interface

The crystallographic arrangement at the interface plays a major role in determining its strength. The strength of the inter-

facial bond is mainly governed by the work of adhesion. HA–CNT interface has been investigated using HRTEM images (Fig. 7). Fourier transform (FFT and inverse-FFT) analysis of the lattice images at interface reveals the presence of CNT and HA. No reaction product was observed at the interface. It is difficult to predict the nature of bonding at HA–CNT interface, due to complex crystal structure of HA. Though the probability of Van der Waal bond is higher between two chemically non-reacting solids like HA and CNT. CNT shows an inter-wall distance of 0.348 nm, which is slightly higher than defect-free CNT inter-wall distance of 0.34 nm. This mismatch is due to the SPS induced defect density in CNT structure as discussed in Section 3.2. HA particles are identified by the lattice spacing of 0.282 nm for the (2 1 1) plane, which produces the 100% intensity peak in XRD pattern of hexagonal HA (Fig. 7).

Two different types of interfaces are possible in HA–CNT system. They are: (i) HA crystals attached to CNT wall and (ii) HA crystals along the CNT end (cross-section). Good interfacial bonding could be achieved only in case of small lattice mismatch (δ) giving rise to minimum lattice strain. Absence of lattice strain improves the ‘work of adhesion’ at the interface, which further increases the fracture energy of the interface and thus makes it strong [63]. The interface becomes incoherent when $\delta > 0.25$ [64]. As observed in Fig. 7, the (2 1 1) planes in HA make 68° angle with CNT walls. The angle

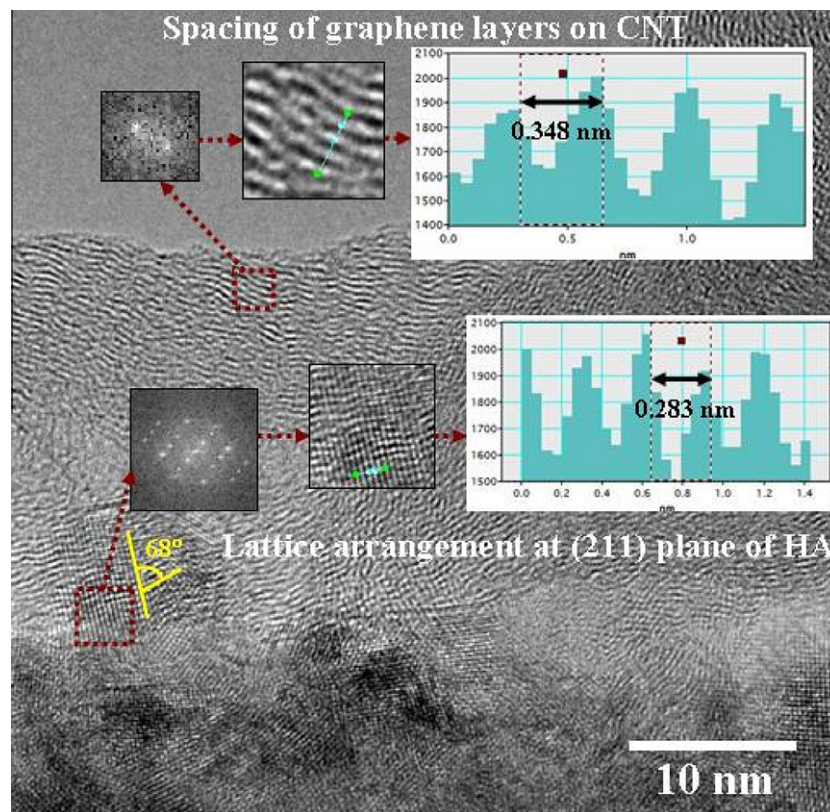


Fig. 7 – HRTEM image of CNT and HA interface. FFT analysis reveals the CNT wall spacing and HA lattice spacing at the interface.

between the basal plane (0 0 1) and (2 1 1) of HA is 65° . Hence, there is a greater possibility that basal planes of HA are parallel to the graphene sheet on CNT wall. Both of them are symmetric in nature due to the hexagonal arrangement of C (CNT) and Ca (HA) atoms. The distance between C atoms in graphene is 0.142 nm. The basal plane of HA has Ca atoms at each corner of the hexagon and the distance between each pair of Ca atom is 0.94 nm. Schematic diagram presented in Fig. 8a shows a HA basal plane superimposed on a graphene sheet. HA crystals try to align on CNT surface resulting in minimum atomic distance mismatch. The distance between carbon atoms (C1 and C2 in Fig. 8a), nearest to the Ca atoms (Ca-1 and Ca-2) along one side of HA basal plane, is 1.026 nm. As the distance between corresponding Ca atoms of HA basal plane (Ca-1 and Ca-2) is 0.94 nm, the mismatch (δ) between the interatomic distance of these two pairs of C and Ca atoms is 0.09, which is much lower than 0.25. Hence, basal plane of HA forms a strong and coherent interfacial bond with the CNT wall. Thus, basal planes of HA crystals prefer to align on the CNT surface. The only disturbance to this strong interfacial bonding is the defects on CNT walls introduced by SPS processing. These defects are probable sites for the CNT debonding from the HA matrix causing pull-outs.

At the open ends of CNT, the concentric walls are exposed with an inter-wall spacing of 0.34 nm. The lattice spacing of (2 1 1), the highest intensity plane of HA (XRD), is 0.282 nm. The lattice mismatch (δ) between (2 1 1) plane of HA and CNT walls is 0.20, which is also lower than 0.25. Thus open

ends of CNT forms a semi-coherent interface with HA crystals with an orientation such that (2 1 1) planes are parallel to CNT walls, as shown in Fig. 8b. The strong and coherent interface with a higher work of adhesion between CNT and HA without other reaction product is the key factor for the improvement of the mechanical properties.

3.4. Effect of CNT reinforcement on improvement in the mechanical properties

3.4.1. Elastic modulus

Measurement of the elastic modulus (E) of the SPS HA and HA–CNT composites has been performed using nanoindentation technique [27,65]. Nanoindentation provides localized mechanical properties. In order to get an impression of the bulk mechanical properties of the composites, more than 100 indents were made at randomly chosen regions throughout the cross-section of the pellets. In each region, the indents were made at a distance of $9\mu\text{m}$ from each other. Total area covered by the indents was $>5000\mu\text{m}^2$ in each sample. The statistical distribution of elastic modulus, measured from individual indents, thus provides the mechanical property of the composite at macro-scale length.

A representative load vs. displacement curve for both HA and HA–CNT is shown in Fig. 9a. Low indentation depth of HA–CNT sample in Fig. 9a indicates higher hardness. Elastic modulus, calculated from the unloading part of the load–displacement curves (Table 2), shows a 25% improvement with

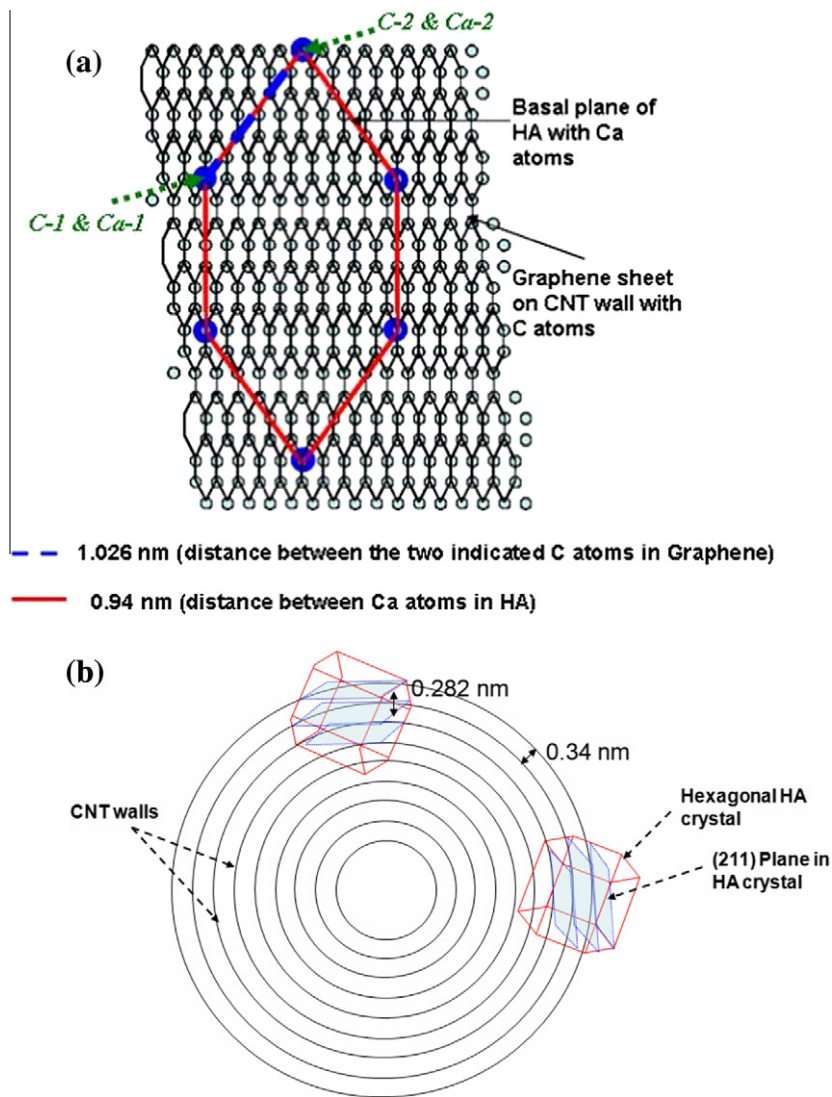


Fig. 8 – (a) Schematic of atomic arrangement at the interface of basal plane of HA and CNT surface and (b) schematic of CNT cross-section showing alignment of CNT walls with (2 1 1) planes of HA.

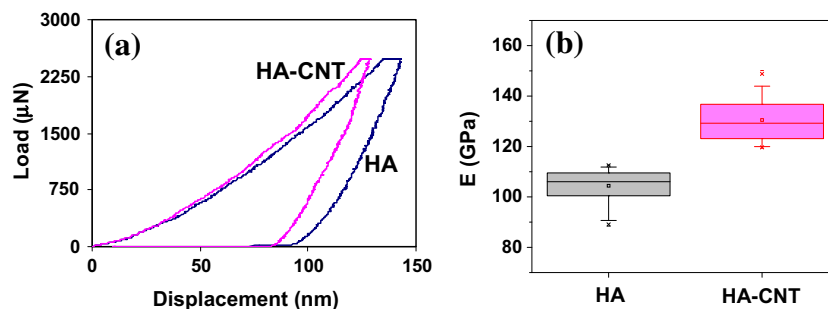


Fig. 9 – (a) Load vs. displacement plot for HA and HA-CNT composite obtained by nanoindentation, (b) statistical distribution of E value in HA and HA-CNT composites measured for more than 100 nanoindents in each sample.

CNT reinforcement in HA. The measured E value of 130 GPa in this study agrees well with the reported E for HA-CNT composite processed through SPS route [39]. The spread in E, as presented in the statistical distribution plot in Fig. 9b, is due

to the localized nature of the measurement technique. Similar amount of spread in E value for both HA and HA-CNT indicates homogeneous improvement in effective elastic modulus at macro-scale length.

Table 2 – Mechanical properties measured by nanoindentation and Vickers indentation methods and calculated through computational models.

Sample	E (GPa) (measured)	E (GPa) (Eshelby)	E (GPa) (Mori–Tanaka)	W_{elas}/W_{tot}	H (GPa) (Vickers)	K_{IC} (MPa m ^{1/2}) (Anstis' equation)
HA	104 ± 6	–	–	0.53	7 ± 0.2	1.25 ± 0.91
HA-4CNT	130 ± 8	159	160	0.64	9 ± 0.4	2.4 ± 0.60

Fraction of the plastic and elastic work during indentation for the composite structure is given by the following expressions [66],

$$W_t = W_e + W_p \quad (4)$$

$$\frac{W_p}{W_t} = 1 - \left[\frac{1 - 3\left(\frac{h_f}{h_m}\right)^2 + 2\left(\frac{h_f}{h_m}\right)^3}{1 - \left(\frac{h_f}{h_m}\right)^2} \right] \quad (5)$$

where W_t , W_p and W_e are the total, plastic and elastic (reversible) work done respectively, h_m is the depth of the indent at the peak load and h_f is the final depth of indentation after recovery. Table 2 shows the fraction of elastic work in HA-CNT increases by 20% than HA. This calculation shows that CNT reinforcement makes the HA matrix more prone to recovery upon deformation.

The increase in the elastic modulus of HA-CNT composite is attributed to three major factors: (i) higher E value of CNT reinforcement (200–1000 GPa [67]), (ii) homogeneous distribution of CNT in HA matrix and (iii) strong HA/CNT interface. The overall effective elastic modulus of the composites has also been computed using Eshelby [68] and Mori–Tanaka [69] micromechanics models. A lower value of E of CNT ~200 GPa was used for these computations as defects have been introduced in the CNT structure during SPS, which will have negative effect on the elastic modulus and tensile strength of a pristine CNT. The computed E values, presented in Table 2, are in the similar range as of experimentally measured E values. The small mismatch between the computed and measured E values could be due to several reasons. Firstly, the effect of porosity present in the composite has not been taken care in the computed model. Secondly, presence of few CNT clusters also causes the localized decrease in E values. Moreover, both the models consider the ellipsoid reinforcement particles, whereas CNTs are tubular in shape.

Good bonding at the HA/CNT interface also plays a role in improving the E for the composite structure. When a stress is applied on a composite material, the matrix deforms first due to lower elastic modulus. A strong matrix/reinforcement interface would resist the selective elastic deformation of matrix by transferring the stress on the reinforcement. Thus, the effective elastic strain generated in the composite matrix reduces with application of elastic stress resulting in an increase in E for the composite. Fig. 10a presents the fracture surface with CNTs protruded from the HA matrix. The protruded CNTs in Fig. 10a shows much shorter length (100–300 nm) compared to the length of CNTs used in this study (1–3 μ m), which indicates a strong bonding between matrix and reinforcement. Strong interfacial bond hinders the sliding between reinforcement and matrix and increases the fiber pull-out stress. As a result, only partial debonding of reinforcement from the matrix occurs, resulting into shorter length of pull-outs. Fig. 10b shows high magnification SEM image of a CNT pull-out. CNT/HA interface shows a very good bonding without any sign of loosening or cracks.

3.4.2. Fracture toughness

Fracture toughness was evaluated using indentation cracking method. Vickers indentation at 1 kg of normal load was employed to initiate cracking in the composite. Fig. 11a and c shows Vickers indents on the cross-sections of HA and HA-CNT pellets, respectively. Indent on HA-CNT shows a smaller impression with shorter radial cracks as compared to HA. The indents were observed at high magnification under SEM for an accurate measurement of the crack lengths. Fracture toughness of the composite structures has been evaluated using Anstis' equation [70] expressed as:

$$K_{IC} = 0.016 \left(\frac{E}{H} \right)^{1/2} \frac{P}{c^{3/2}} \quad (6)$$

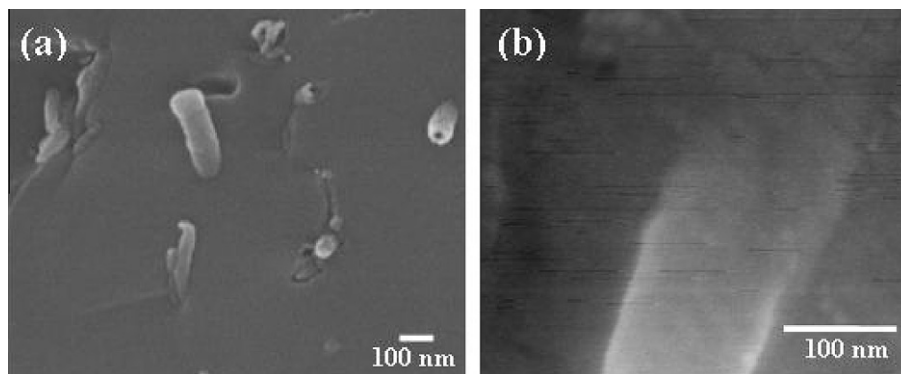


Fig. 10 – High magnification SEM micrographs of HA-CNT fracture surface showing (a) protruded CNTs and (b) strong and defect-free interface of CNT with HA matrix.

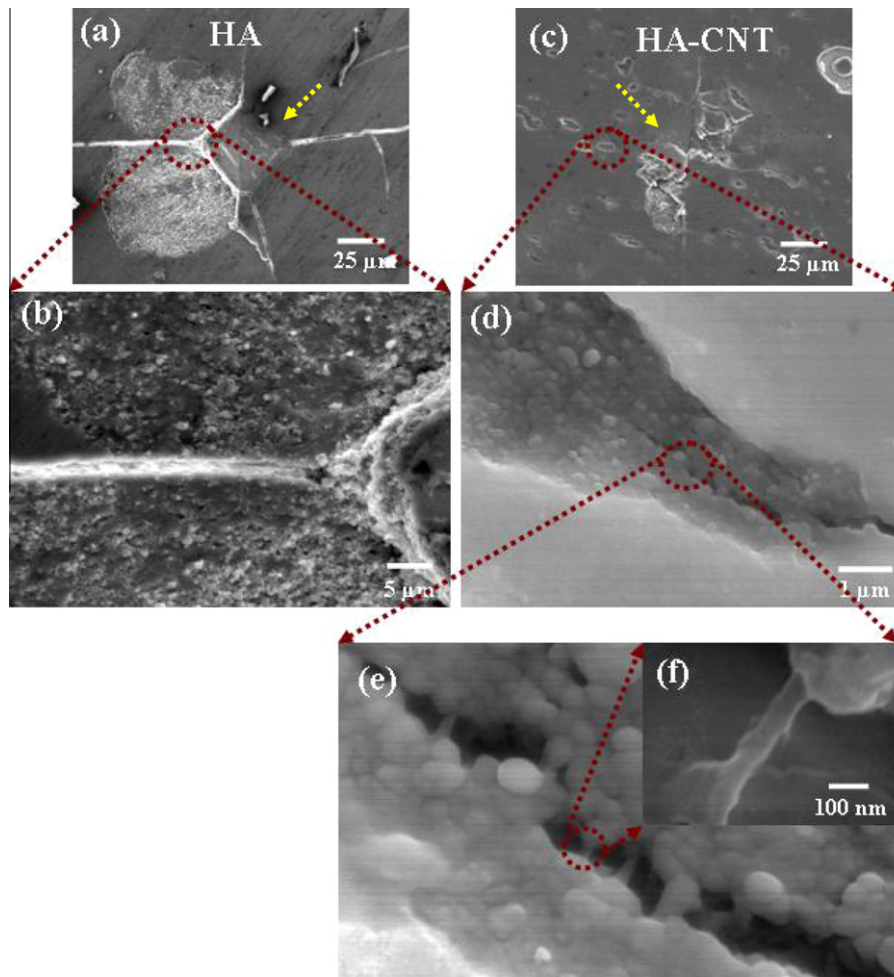


Fig. 11 – SEM micrographs of polished cross-sections in HA and HA-CNT showing (a) Vicker's indents impression on HA and (b) radial crack from the indent propagating in fine grain region of HA, (c) Vicker's indents impression on HA-CNT, (d) deflection and arrest of radial crack at fine grain region in HA-CNT, (e) crack bridging by CNT and (f) high magnification image of a single CNT bonded with HA matrix at both ends and forming bridge on crack.

where P is the applied load, E is the elastic modulus, H is the Vickers hardness and c is the radial crack length (measured from the centre of the indent). E values measured by nanoindentation were used to compute K_{IC} of the composite. K_{IC} shows a 92% improvement with CNT addition in HA, whereas hardness increases by 29% (Table 2). K_{IC} , calculated for HA-CNT composite in this study ($2.4 \text{ MPa m}^{0.5}$) is much higher than the only available literature value of $1.27 \text{ MPa m}^{0.5}$ [38]. The improvement of K_{IC} in the same study is 30%, which is much less than 92% improvement reported in this study. One of the probable reasons is the lower content of CNT (2.5 vol.%) used in Ref. [38], as compared to this study (4 wt.% \approx 6 vol.% CNT). Further, the use of spray-dried HA-CNT composite powder in this study ensures the better distribution and good bonding of CNT with matrix in the sintered structure. The detrimental effect of few CNT clusters was minimal in comparison to the benefits from uniformly dispersed CNTs. Detailed SEM investigations inside the indentation cracks reveal two factors responsible for the improvement in fracture toughness of HA-CNT composite. One of them is the resistance to crack propagation at fine grain region of HA-CNT composite. Fig. 11c shows the deflec-

tion and arrest of crack at fine grained region in HA-CNT. In contrast, HA fine grain region does not arrest the crack as shown in Fig. 11b. This is attributed to the difference in the densification level of the fine grain region in HA and HA-CNT. HA-CNT composite has high fraction of fine grained region (discussed in Section 3.1), causing the crack propagation more difficult. The second mechanism that resists the crack propagation is CNT-bridging. High magnification SEM micrographs inside the cracks (Fig. 11e and f) show individual CNTs forming bridges on the crack and resisting its propagation.

Further evaluation of toughening mechanism in HA-CNT composite has been studied using a model developed by Chen et al. that computes interfacial shear strength and reinforcement pull-out energy for CNT-ceramic composites [71]. The effective area of load carrying outer layers (A_{eff}) of multiwall CNTs has been calculated using the following expression:

$$A_{eff} = \pi \sum_{m=1}^N \left\{ [R_{CNT} - (m-1)h - (m-1)h']^2 - [R_{CNT} - mh - (m-1)h']^2 \right\} \quad (7)$$

where R_{CNT} is the outer radius of CNT (25–50 nm in this study), h is the effective layer (wall) thickness ($\sim 0.075 \text{ nm}$), d is the

spacing between each graphene layer (~ 0.34 nm) and $h' = d - h$, and N is the number of outer layers carrying load. The CNTs used in this study has 28–51 graphene layers (measured from HRTEM images). But, the CNTs having SPS induced defects, only the outer five layers have been considered as active load carrying components in this calculation. Cox model has been used to compute the interfacial shear strength (τ) between HA and CNT. Cox model assumes the fiber at the centre of a coaxial cylinder of the matrix (of radius R) to calculate τ , which is expressed as following:

$$\tau = \frac{E_{CNT} \times e \times A_{eff} \times \beta}{2\pi R_{CNT}} \times \frac{\sinh \beta \left(\frac{l}{2} - x\right)}{\cosh \beta \frac{l}{2}} \quad (8)$$

where

$$\beta = \sqrt{\left(\frac{G'_{HA}}{E_{CNT}}\right) \left(\frac{2\pi}{A_{eff} \ln \left(\frac{R}{R_{CNT}}\right)}\right)} \quad (9)$$

E_{CNT} is the elastic modulus of CNT, used as 200 GPa for this study. The applied strain e has been taken as 0.04, the fracture strain of HA [72]. L is the length of CNT, which is 1–3 μ m in this study and x is the distance from end of CNT. $G'_{HA} \sim 45$ GPa [73,74] is the shear modulus of HA. The radius of matrix coaxial cylinder, R , has been calculated using the following relationship,

$$\left(\frac{R}{R_{CNT}}\right)^2 = \frac{\pi}{4V_f} \quad (10)$$

$V_f \sim 6$, is the volume fraction of CNT in HA matrix. The calculated interfacial shear stress at HA–CNT interface, τ , is 0.3–0.35 GPa. Hence, a shear stress greater than this value has to be applied to interface in-order to cause CNT debonding from HA matrix. The computed τ has been used in calculation of pull-out energy ($G_{pullout}$) for HA–CNT system [71], using Eq. (11).

$$G_{pullout} = \frac{V_f l^2 \tau}{3R_{CNT}} \quad (11)$$

where l is the pull-out length of CNTs (100–300 nm) measured from SEM images. The computed $G_{pullout}$ for CNT from HA matrix is 1.5–22 J/m². The fracture energy for monolithic HA is 1 J/m² [75]. The CNT pull-out energy being higher than fracture energy of HA, cracks propagate through HA, but gets restricted when comes in the vicinity of CNT, as more energy is required for interface debonding. Hence, CNT bridges (Fig. 11e and f) absorb more energy and provide resistance to crack growth. Chen et al. has also observed crack deflection at the alumina–CNT composite due to debonding of CNT from matrix prior to fracture in matrix [71].

3.5. Effect of CNT reinforcement on tribological behavior

This study reports the macro- and nano-scale tribological behavior of the SPS processed HA–CNT composite for the first time. Macro-scale wear was conducted using a ball-on-disk tribometer whereas nano-scale wear was evaluated using nano-scratch studies using a nanoindenter.

3.5.1. Macro-scale wear

The wear resistance has been defined in terms of volume loss of the wear track at different traverse distances. The

instantaneous depth of wear track is measured using 'linear variable differential transformer' (LVDT). The cumulative volume loss and coefficient of friction (CoF) for HA and HA–CNT composite are shown in Fig. 12a and b, respectively. Each point in Fig. 12b shows an average value of CoF for 25 m interval. The error bars in Fig. 12 are based on three wear tracks studied for each sample. Wear resistance increases by 66%, whereas CoF decreases by 60% with CNT addition in HA.

The decrease in CoF for HA–CNT indicates more lubrication in the wear track, which could be due to graphene layer removal from CNT by application of shearing force during macro-wear. This assumption is indirectly supported by the change in the relative intensity of D and G peaks of CNT in Raman spectroscopy plots of wear track (Fig. 6a). The I_D/I_G ratio increases from 0.72 in SPS HA–CNT pellet to 1.28 in the wear track of the same sample. Increase in I_D/I_G ratio indicates more defects getting introduced in the CNTs during wear, which is resulted from tearing off of graphene layers. Further, a shift of D and G peak of CNT towards lower wave number is also observed in the wear track, which is attributed to the tensile stress present due to shearing force applied on wear track [76–78]. The shift of the D and G peaks to lower wave numbers is best understood on the basis of an elongation of the carbon–carbon bonds under tension, which make the bond weaker and therefore lowers the vibrational frequency [76]. Same is true for the phosphate peak of HA in wear track also. The extent of shift is more in D and phosphate peaks than in G peak. This is because G peak undergoes a shift to higher wave number due to increase in defect density [60] and simultaneously to lower wave number due to tensile stress induced in it. Hence, the observed shift in G peak is the resultant of these two opposing effects. Increase in the defect density in CNTs during wear is visually observed from the SEM micrographs in Fig. 12c and d, showing presence of damaged and broken CNTs in the wear track. Graphene layer peeling from CNTs by application of shear force is in agreement with a study by Li et al. on SPS consolidated structure [79]. The peeled-off graphene layers cover the wear track, thus providing lubrication and decreasing the coefficient of friction. CNT clusters provide more lubrication due to increased probability of graphene layer formation.

Increase in the wear resistance for HA–CNT composite is a combined effect of improvement in the mechanical properties (E , H and K_{IC}) caused by CNT reinforcement and decrease in the coefficient of friction. Improvement in E , H and K_{IC} increases the resistance to removal of mass with the same amount of applied load. At the same time, decrease in CoF (ratio of lateral and normal force) decreases the effective lateral force in the wear track for the same amount of normal force. In this study, the effective lateral force in HA–CNT is as low as 2.5 N, compared to ~ 7 N in HA sample, due to decrease in CoF. Decrease in the lateral force due to graphite induced lubrication causes lesser wear volume loss in case of HA–CNT.

3.5.2. Nano-scale wear

Nano-scale tribological properties of HA and HA–CNT composite have been measured by making nano-scratches with different normal loads. The volume loss has been calculated from the geometry of scratch profile obtained through

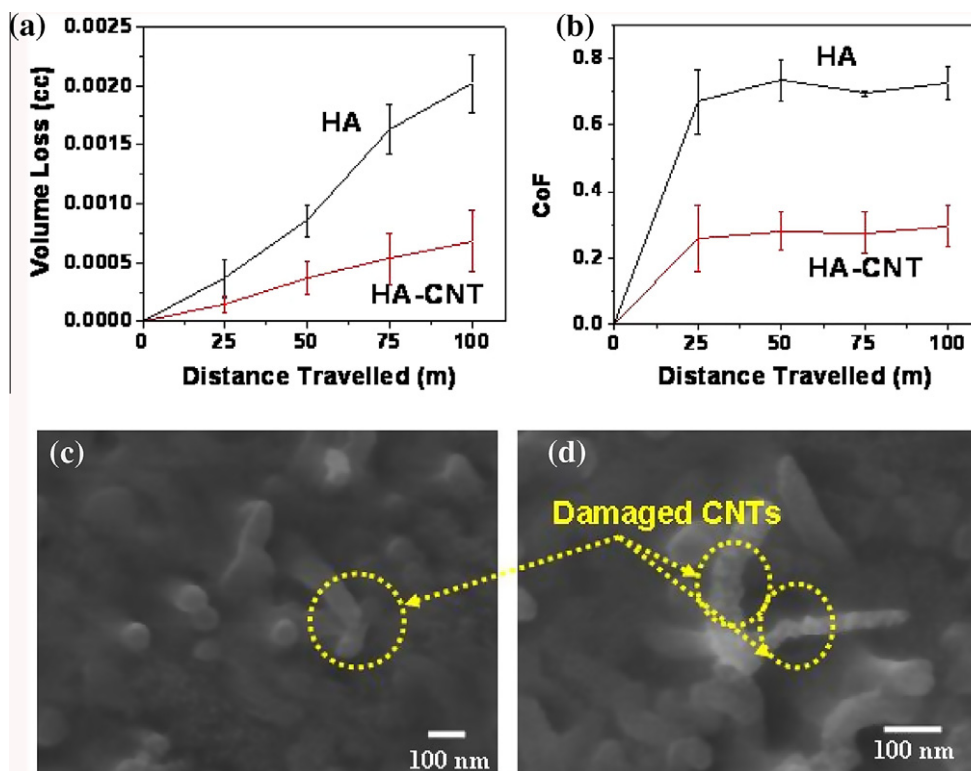


Fig. 12 – (a) Wear volume loss and (b) coefficient of friction for HA and HA-CNT plotted against sliding distance during ball-on-disk wear (c and d) high magnification SEM micrographs of broken and damaged CNTs observed in the HA-CNT wear track.

SPM imaging of the scratch after elastic recovery has taken place, using the following expression:

$$V = \int_0^l h^2 \tan \theta \cdot dl \quad (12)$$

where V is the volume of the scratched-groove, h is the height of the groove (obtained from 2D SPM profile of scratch along the length), θ is the average angle of the groove measured at five points along the scratch length using 2D SPM profile and l is the length of the scratch. The detailed procedure of the volume measurement is explained in a study by Bakshi et al. [46].

Fig. 13a and b shows the wear volume loss and CoF, respectively, for HA and HA-CNT at normal loads of 3500 μN and 4500 μN . The error bars in Fig. 13 are based on three scratches made at each load on each sample. Wear volume loss increases with increase in load and is $\sim 45\%$ higher for HA for both the loads. CoF remains similar at different loads in each of the compositions, but HA-CNT shows 14% increase in CoF. Decrease in the wear volume loss for HA-CNT indicates its higher wear resistance, which is due to the improvement in E , H and K_{IC} as discussed in case of macro-wear (Section 3.4.1). Increase in CoF in HA-CNT indicates the absence of any significant lubrication in case of nano-wear.

Another important observation from the nano-scratch study is the effect of CNT addition on the recovery of HA matrix, which has been calculated using depth of the scratched-groove during scratch and after recovery. HA-CNT shows increase in the recovery at both 3500 μN and 4500 μN loads suggesting higher elastic deformation in the presence

of CNTs (Fig. 13c). This observation directly matches with the higher fraction of elastic work in HA-CNT as calculated from the nanoindentation studies (Table 2).

3.5.3. Differential role of CNT at varying length scales

The tribological properties, reported for HA and HA-CNT composite, show distinct difference in CoF and wear resistance at macro- and nano-scale length. With CNT addition, CoF decreases by 60% in case of macro-wear, whereas it increases by 14% for nano-wear. Further, macro-wear shows 66% increase in the wear resistance with CNT reinforcement, whereas nano-wear study reveals 45% increase in the wear resistance.

Increase in CoF in the case of macro-wear results from the lubrication offered by peeled graphene layers from the CNT walls. Lower lubrication in nano-wear is attributed to the absence of damage and breaking of CNT walls. The effective lateral stress exerted on the CNT walls during macro- and nano-scale further elucidates this phenomenon. Effective lateral stress on the sample surface is same as the stress on the wear probe in contact with sample during removal of mass. The contact area of probe with the sample surface, is referred as effective surface area (SA_{eff}). Fig. 14 shows a schematic for the calculation of SA_{eff} for Berkovich indenter tip used for the nano-wear study. The three sided pyramid shape of Berkovich tip has been approximated to a conical shape, keeping the aspect ratio of height to base (1:8) same. For the scratches made with 4500 μN normal load, the average depth of scratch is 300 nm which corresponds to SA_{eff} as $4.66 \mu\text{m}^2$. The CoF for the same case being 0.29, the lateral force for the scratch is

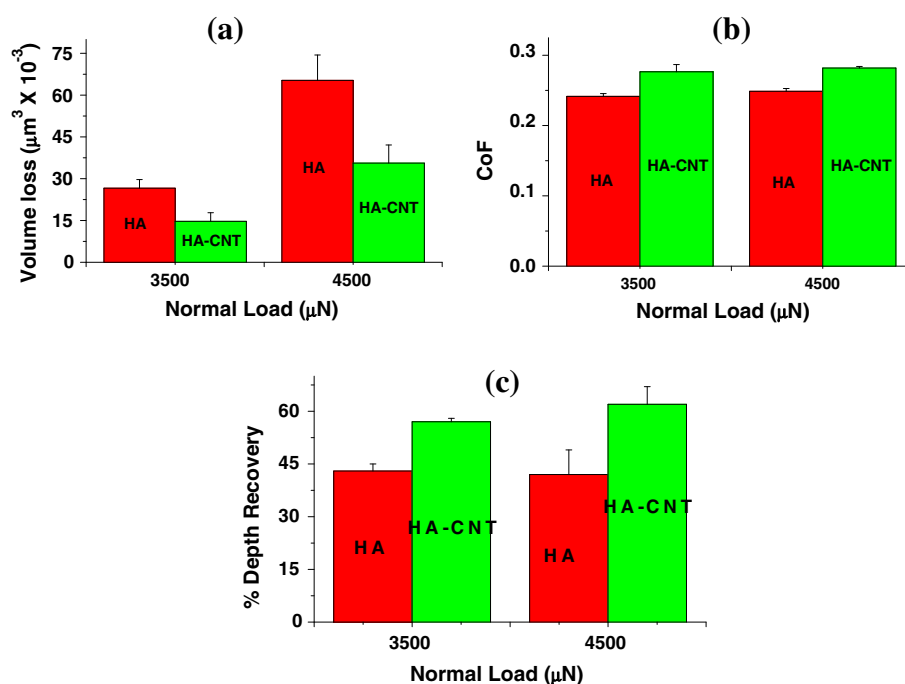


Fig. 13 – Nano-scale (a) wear volume loss and (b) coefficient of friction and (c) percentage elastic depth recovery during nano-scratch of HA and HA-CNT as a function of normal load.

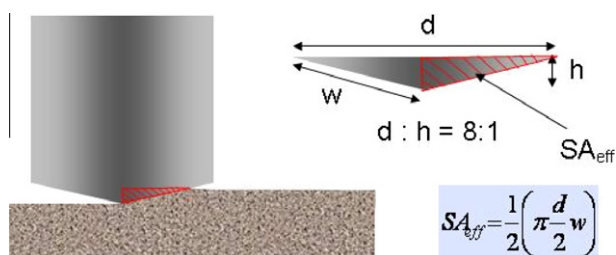


Fig. 14 – Schematic diagram showing the SA_{eff} for nano-scratch study.

$\sim 1300 \mu\text{N}$. These conditions generate a stress of 300 MPa at the Berkovich tip surface in contact with the HA-CNT sample.

In the case of macro-wear, the normal force applied is 10 N. The CoF being 0.25, the effective lateral force on the wear track is 2.5 N. Maximum wear depth achieved in the track is 0.097 mm. For a total wear distance of 100 m, it takes 8×10^3 revolutions in a 2 mm radius wear track. Hence, the average wear depth increase per revolution is 1.25×10^{-5} mm. A 3 mm diameter alumina ball has been used as wear probe. Schematic in Fig. 15 presents the SA_{eff} for macro-wear. The wear depth per revolution being very small with respect to the radius of wear probe, the surface area of sphere has been approximated to the circular area of the truncated sphere as shown in Fig. 15. The SA_{eff} , thus calculated, is $1.18 \times 10^{-4} \text{ mm}^2$. Hence, the lateral stress achieved in case of macro-wear is $\sim 21 \text{ GPa}$.

These calculations show that macro-wear applies 70 times higher lateral stress on wear track than nano-wear. Yu et al. have reported that removal of a single graphene layer from multiwall CNT requires a tensile force in range of 11–63 GPa,

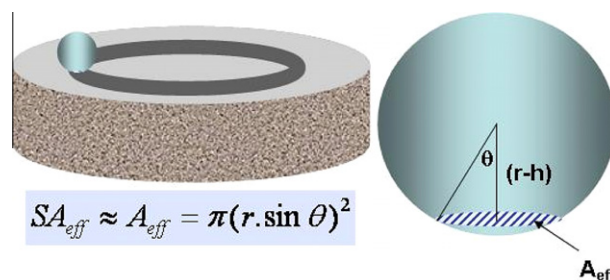


Fig. 15 – Schematic diagram showing the SA_{eff} for macro-wear study.

with varying OD and length of nanotubes [80]. Lateral force during wear causes shearing removal of mass on the surface, which causes tensile stress on the newly exposed surface after mass removal. As the force applied in nano-wear (300 MPa) is much smaller than the minimum stress required for graphene layer peeling from CNT (11 GPa), no lubrication is available in this case. On the contrary, the available lateral stress in case of macro-wear (21 GPa) is enough to remove graphene layer which causes a significant decrease in CoF. Increase in the lubrication also contributes towards increasing wear resistance for HA-CNT.

4. Conclusion

HA-CNT composite, with improved mechanical and tribological properties, has been successfully fabricated through SPS processing. Rapid heating rate for SPS processing, used in this study (360 K/min), prohibits the dissociation of HA into TCP. Good electrical and thermal conductivity of CNT play

important roles in improved densification of microstructure in HA–CNT composite. CNTs also pin the grain boundaries and retain HA nanostructure, which helps in improving the elastic modulus and fracture toughness. A 92% increase in the fracture toughness of HA–CNT was obtained due to a combined effect of improved modulus, higher fraction of nanocrystalline HA region and crack bridging by CNTs. Macro-scale dry sliding wear of HA–CNT composite showed a 66% improvement in the wear resistance and 60% reduction in CoF as compared to HA. Increase in the wear resistance is due to improvement in mechanical properties (E , H and K_{IC}) as well as decrease in CoF for HA–CNT. The decrease in CoF is due to peeling of graphene layer from CNT surface that provides lubrication. In case of nano-scale wear, a 45% increase in the wear resistance is observed. Nano-scale CoF increase by 14% in presence of CNTs, due to absence of lubrication from graphene layer peeling. The effective shear stress during macro-wear causes graphene layers to peel-off from CNTs. The effective shear stress in nano-wear is significantly lower than the minimum stress required for removing a graphene layer from CNT surface.

Acknowledgements

Authors acknowledge support from the research facility at Advanced Materials Engineering and Research Institute (AMERI) in Florida International University and Mr. Neal Ricks, manager, AMERI. The authors are thankful to the Center for study of Matters in Extreme Conditions (CeSMEC) and Dr. S. Saxena for extending the use of Micro Raman Spectroscopy facility. A.A. acknowledges funding from the National Science Foundation CAREER Award (NSF-DMI-0547178) and Office of Naval Research–DURIP program (N00014-06-0675). D.L. acknowledges support from the Dissertation Evidence Acquisition Fellowship and A.K.K. from the Dissertation Year Fellowship by University Graduate School of Florida International University.

REFERENCES

- [1] Gu YW, Loha NH, Khor KA, Tor SB, Cheang P. Spark plasma sintering of hydroxyapatite powders. *Biomaterials* 2002;23:37–43.
- [2] Yu LG, Khor KA, Li H, Cheang P. Effect of spark plasma sintering on the microstructure and in vitro behavior of plasma sprayed HA coatings. *Biomaterials* 2003;24:2695–705.
- [3] White AA, Best SM, Kinloch IA. Hydroxyapatite–carbon nanotube composites for biomedical applications: a review. *Int J Appl Ceram Technol* 2007;4(1):1–13.
- [4] Tas AS. Synthesis of biomimetic Ca–hydroxyapatite powders at 373 °C in synthetic body fluids. *Biomaterials* 2000;21:1429–38.
- [5] Gu YW, Khor KA, Cheang P. Bone-like apatite layer formation on hydroxyapatite prepared by spark plasma sintering (SPS). *Biomaterials* 2004;25:4127–34.
- [6] Balani K, Chen Y, Harimkar SB, Dahotre NB, Agarwal A. Tribological behavior of plasma-sprayed carbon nanotube-reinforced hydroxyapatite coating in physiological solution. *Acta Biomater* 2007;3:944–51.
- [7] Chen Y, Zhang TH, Gun CH, Yu G. Wear studies of hydroxyapatite composite coating reinforced by carbon nanotubes. *Carbon* 2007;45:998–1004.
- [8] Li H, Khor KA, Chow V, Cheang P. Nanostructural characteristics, mechanical properties, and osteoblast response of spark plasma sintered hydroxyapatite. *J Biomed Mater Res A* 2007;82:296–303.
- [9] Guo X, Gough JE, Xiao P, Liu J, Shen Z. Fabrication of nanostructured hydroxyapatite and analysis of human osteoblastic cellular response. *J Biomed Mater Res A* 2007;82:1022–32.
- [10] Que W, Khor KA, Xu JL, Yu LG. Hydroxyapatite/titania nanocomposites derived by combining high-energy ball milling with spark plasma sintering processes. *J Eur Ceram Soc* 2008;28:3083–90.
- [11] Grossin D, Rollin-Martinet S, Estournès C, Rossignol F, Champion E, Combes C, et al. Biomimetic apatite sintered at very low temperature by spark plasma sintering: physico-chemistry and microstructure aspects. *Acta Biomater* 2010;6:577–85.
- [12] Wang W, Chen J, Agarwal DK, Malshe AP, Liu H. Improved mechanical properties of nanocrystalline hydroxyapatite coating for dental and orthopedic implants. *Mater Res Soc Symp Proc* 2009;1140. doi:10.1557/PROC-1140-HH03-03.
- [13] Seal S, Kuiry SC, Georgieva P, Agarwal A. Manufacturing nanocomposite parts: present status and future challenges. *Mater Res Soc Bull* 2004;29(1):16–21.
- [14] Viswanathan V, Laha T, Balani K, Agarwal A, Seal S. Challenges and advances in nanocomposite processing techniques. *Mater Sci Eng R* 2006;54(5–6):121–285.
- [15] Lu K. Sintering of nanoceramics. *Int Mater Rev* 2008;53(1):21–37.
- [16] Chaim R, Levin M, Shlayer A, Estournes C. Sintering and densification of nanocrystalline ceramic oxide powders: a review. *Adv Appl Ceram* 2008;107(3):159–69.
- [17] Ragulya AV. Consolidation of ceramic nanopowders. *Adv Appl Ceram* 2008;107(3):118–34.
- [18] Munir ZA, Tamburini UA, Ohyanagi M. The effect of electric field and pressure on the synthesis and consolidation of materials: a review of the spark plasma sintering method. *J Mater Sci* 2006;41:763–77.
- [19] Olevsky EA, Kandukuri S, Froyen L. Consolidation enhancement in spark-plasma sintering: impact of high heating rates. *J Appl Phys* 2007;102:114913 (1–12).
- [20] Xu JL, Khor KA, Kumar R. Physicochemical differences after densifying radio frequency plasma sprayed hydroxyapatite powders using spark plasma and conventional sintering techniques. *Mater Sci Eng A* 2007;457:24–32.
- [21] Li S, Izui H, Okano M. Densification, microstructure and behavior of hydroxyapatite ceramics sintered by using spark plasma sintering. *J Eng Mater Technol* 2008;130:031012.1–7.
- [22] Ma RZ, Wu J, Wei BQ, Wu DH. Processing and properties of carbon nanotubes–nano-SiC ceramic. *J Mater Sci* 1998;33:5243–6.
- [23] Siegel RW, Chang SK, Ash BJ, Stone J, Ajayan PM, Doremus RW, et al. Mechanical behavior of polymer and ceramic matrix nanocomposites. *Scr Mater* 2001;44:2061–4.
- [24] Zhan GD, Kuntz JD, Wan J, Mukherjee AK. Single-wall carbon nanotubes as attractive toughening agents in alumina-based nanocomposites. *Nat Mater* 2003;2(1):38–42.
- [25] Balani K, Zhang T, Karakoti A, Li WZ, Seal S, Agarwal A. In situ carbon nanotube reinforcements in a plasma-sprayed aluminum oxide nanocomposite coating. *Acta Mater* 2008;56:571–9.
- [26] Balani K, Anderson R, Laha T, Andara M, Tercero J, Crumpler E, et al. Plasma-sprayed carbon nanotube reinforced hydroxyapatite coatings and their interaction with human osteoblasts in vitro. *Biomaterials* 2007;28:618–24.

- [27] Balani K, Lahiri D, Keshri AK, Bakshi SR, Tercero JE, Agarwal A. The nano-scratch behavior of biocompatible hydroxyapatite reinforced with aluminum oxide and carbon nanotubes. *JOM* 2009;61(9):63–6.
- [28] Tercero JE, Namin S, Lahiri D, Balani K, Tsoukias N, Agarwal A. Effect of carbon nanotube and aluminum oxide addition on plasma-sprayed hydroxyapatite coating's mechanical properties and biocompatibility. *Mater Sci Eng C* 2009;29:2195–202.
- [29] Chen Y, Gan C, Zhang T, Yu G, Bai P, Kaplan A. Laser-surface-alloyed carbon nanotubes reinforced hydroxyapatite composite coatings. *Appl Phys Lett* 2005;86:251905 (1–3).
- [30] Singh I, Kaya C, Shaffer MSP, Thomas BC, Boccaccini AR. Bioactive ceramic coatings containing carbon nanotubes on metallic substrates by electrophoretic deposition. *J Mater Sci* 2006;41:8144–51.
- [31] Kaya C, Singh I, Boccaccini AR. Multi-walled carbon nanotube-reinforced hydroxyapatite layers on Ti6Al4V medical implants by electrophoretic deposition (EPD). *Adv Eng Mater* 2008;10(1–2):131–8.
- [32] Hahn BD, Lee JM, Park DS, Choi JJ, Ryu J, Yoon WH, et al. Mechanical and in vitro biological performances of hydroxyapatite–carbon nanotube composite coatings deposited on Ti by aerosol deposition. *Acta Biomater* 2009;5:3205–14.
- [33] Li A, Sun K, Dong W, Zhao D. Mechanical properties, microstructure and histocompatibility of MWCNTs/HAp biocomposites. *Mater Lett* 2007;61:1839–44.
- [34] Li H, Zhao N, Liu Y, Liang C, Shi C, Du X, et al. Fabrication and properties of carbon nanotubes reinforced Fe/hydroxyapatite composites by in situ chemical vapor deposition. *Composite A* 2008;39:1128–32.
- [35] Kealley C, Ben-Nissan B, Van Riessen A, Elcombe M. Development of carbon nanotube reinforced hydroxyapatite bioceramics. *Key Eng Mater* 2006;309–311:597–600.
- [36] Kealley C, Elcombe M, Riessen A, Ben-Nissan B. Development of carbon nanotube-reinforced hydroxyapatite bioceramics. *Physica B* 2006;385–386:496–8.
- [37] Omori M, Okubo A, Otsubo M, Hashida T, Tohji K. Consolidation of multi-walled carbon nanotube and hydroxyapatite coating by the spark plasma system (SPS). *Key Eng Mater* 2004;254–256:395–8.
- [38] Sarkar SK, Youn MH, Oh IH, Lee BT. Fabrication of CNT reinforced HAp composites by spark plasma sintering. *Mater Sci Forum* 2007;534–536:893–6.
- [39] Xu JL, Khor KA, Sui JJ, Chen WN. Preparation and characterization of a novel hydroxyapatite/carbon nanotubes composite and its interaction with osteoblast-like cells. *Mater Sci Eng C* 2009;29:44–9.
- [40] Fioritto S. Carbon nanotubes: angels or demons? Singapore: Pan Stanford; 2008. ISBN: 981424 1016, 9789814241014.
- [41] Singh R, Pantarotto D, Lacerda L, Pastorin G, Klumpp C, Prato M, et al. Tissue biodistribution and blood clearance rates of intravenously administered carbon nanotube radiotracers. *Proc Natl Acad Sci* 2006;103(9):3357–62.
- [42] Usui Y, Aoki K, Narita N, Murakami N, Nakamura I, Nakamura K, et al. Carbon nanotubes with high bone-tissue compatibility and bone-formation acceleration effects. *Small* 2008;4(2):240–6.
- [43] Cheng C, Muller KH, Koziol KK, Skepper JN, Midgley PA, Welland ME, et al. Toxicity and imaging of multi-walled carbon nanotubes in human macrophage cells. *Biomaterials* 2009;30:4152–60.
- [44] Balani K, Bakshi SR, Chen Y, Laha T, Agarwal A. Role of powder treatment and carbon nanotube dispersion in the fracture toughening of plasma-sprayed aluminum oxide–carbon nanotube nanocomposite. *J Nanosci Nanotechnol* 2007;7(10):1–10.
- [45] Oliver WC, Pharr GM. An improved technique for determining hardness and elastic modulus using load and displacement sensing indentation experiments. *J Mater Res* 1992;7(6):1564–83.
- [46] Bakshi SR, Lahiri D, Patel R, Agarwal A. Nanoscratch behavior of carbon nanotube reinforced aluminum coatings. *Thin Solid Films* 2009. doi:10.1016/j.tsf.2009.11.079.
- [47] Shen Z, Nygren M. Microstructural prototyping of ceramics by kinetic engineering: applications of spark plasma sintering. *Chem Rec* 2005;5:173–84.
- [48] Gaona M, Lima RS, Marple BR. Nanostructured titania/hydroxyapatite composite coatings deposited by high velocity oxy-fuel (HVOF) spraying. *Mater Sci Eng A* 2007;458:141–9.
- [49] Laghzeil A, El Herch N, Bouhaouss A, Lorente G, Macquete J. Comparison of electrical properties between fluoroapatite and hydroxyapatite materials. *J Solid State Chem* 2001;156:57–60.
- [50] Che J, Cagin T, Goddard III WA. Thermal conductivity of carbon nanotubes. *Nanotechnology* 2000;11:65–9.
- [51] Ebbesen TW, Lezec HJ, Hiura H, Bennett JW, Ghaemi HF, Thio T. Electrical conductivity of individual nanotubes. *Nature* 1996;382:54–6.
- [52] Miodownik M, Holm EA, Hassold GN. High parallel computer simulations of particle pinning: Zener vindicted. *Scr Mater* 2000;42:1173–7.
- [53] Sun N, Patterson BR, Suni JP, Weiland H, Allard LF. Characterization of particle pinning potential. *Acta Mater* 2006;54:4091–9.
- [54] Kim BC, Lee JH, Kim JJ, Ikegami T. Rapid rate sintering of nanocrystalline indium tin oxide ceramics: particle size effect. *Mater Lett* 2002;52:114–9.
- [55] Kim H, Camata RP, Lee S, Rohrer GS, Rollett AD, Vohra YK. Crystallographic texture in pulsed laser deposited hydroxyapatite bioceramic coatings. *Acta Mater* 2007;55:131–9.
- [56] Roomie CM, Craig CD. Crystallite orientation and anisotropic strains in thermally sprayed hydroxyapatite coatings. *Biomaterials* 1995;16:691–6.
- [57] Kim H, Camata RP, Chowdhury S, Vohra YK. In-vitro dissolution and mechanical behavior of c-axis preferentially oriented hydroxyapatite thin films fabricated by pulsed laser deposition. *Acta Biomater*. doi: 10.1016/j.actbio.2010.02.031.
- [58] Dresselhaus MS, Dresselhaus G, Saito R, Jorio A. Raman spectroscopy of carbon nanotubes. *Phys Rep* 2005;409:47–99.
- [59] Liu J, Glasmacher UA, Lang M, Trautman C, Voss KO, Neumann R, et al. Raman spectroscopy of apatite irradiated with swift heavy ions with and without simultaneous exertion of high pressure. *Appl Phys A* 2008;9:17–22.
- [60] Das A, Chakraborty B, Sood AK. Raman spectroscopy of graphene on different substrates and influence of defects. *Bull Mater Sci* 2008;31(3):579–84.
- [61] Yang K, He J, Su Z, Reppert JB, Skove MJ, Tritt TM, et al. Inter-tube bonding, graphene formation and anisotropic transport properties in spark plasma sintered multi-wall carbon nanotube arrays. *Carbon* 2010;48:756–62.
- [62] Bakshi SR, Singh V, McCartney DG, Seal S, Agarwal A. Deformation and damage mechanisms of multiwalled carbon nanotubes under high-velocity impact. *Scr Mater* 2008;59:499–502.
- [63] Messerschmidt U, Bartsch M, Dietsch C, Kurtz W, Scheu C, Rühle M. HVEM in situ study of fracture of Al₂O₃/Nb sandwich specimen. *Z Metallkd* 2004;95(9):785–92.
- [64] Porter DA, Easterling KE. Phase transformation in metals and alloys. 2nd ed. Cheltenham, UK: CRC Press; 2001. p. 142–69.
- [65] Agarwal A, Dahotre N. Mechanical properties of laser-deposited composite boride coating using nanoindentation. *Metall Trans A* 2000;31(2):401–8.

-
- [66] Cheng YT, Cheng CM. Scaling, dimensional analysis, and indentation measurements. *Mater Sci Eng R* 2004;44:91–149.
- [67] Singh S, Pei Y, Miller R, Sundararajan PR. Long-range, entangled carbon nanotube networks in polycarbonate. *Adv Funct Mater* 2003;13(11):868–72.
- [68] Eshelby JD. The determination of elastic field of an ellipsoidal inclusion, and related problems. *Proc R Soc London* 1957;241:376–96.
- [69] Mori T, Tanaka K. Average stress in matrix and average elastic energy of materials with misfitting inclusions. *Acta Metall* 1973;21:571–4.
- [70] Anstis GR, Chantikul P, Lawn BR, Marshall DB. A critical evaluation of indentation techniques for measuring fracture toughness: I. Direct crack measurements. *J Am Ceram Soc* 1981;64(9):533–8.
- [71] Chen Y, Balani K, Agarwal A. Analytical model to evaluate interface characteristics of carbon nanotube reinforced aluminum oxide nanocomposites. *Appl Phys Lett* 2008;92:011916 (1–3).
- [72] Pramanik S, Agarwal AK, Rai KN. Development of high strength hydroxyapatite for hard tissue replacement. *Trends Biomater Artif Organs* 2005;19(1):46–51.
- [73] Hellmich C, Ulm FJ. Poro-micromechanics of bone: impact loading and wave propagation. In: *Mechanical properties of bioinspired and biological materials*, MRS 2004 Fall Meeting, Boston, USA. *Mater Res Soc Symp Proc* 2005;844:Y8.6.1–7.
- [74] Fritsch A, Dormieux L, Hellmich C, Sanahuja J. Mechanical behavior of hydroxyapatite biomaterials: an experimentally validated micromechanical model for elasticity and strength. *J Biomed Mater Res* 2009;88A:149–61.
- [75] Nakahira A, Eguchi K. Evaluation of microstructure and some properties of hydroxyapatite/Ti composites. *J Ceram Proc Res* 2001;2(3):108–12.
- [76] Cronin SB, Swan AK, Unlu MS, Goldberg BB, Dresselhaus MS, Tinkham M. Measuring the uniaxial strain of individual single-wall carbon nanotubes: resonance Raman spectra of atomic-force-microscope modified single-wall nanotubes. *Phys Rev Lett* 2004;93 (16):167401(1–4).
- [77] Bakshi SR, Tercero JE, Agarwal A. Synthesis and characterization of multiwalled carbon nanotube reinforced ultra high molecular weight polyethylene composite by electrostatic spraying technique. *Composites A* 2007;38:2493–9.
- [78] Mu M, Osswald S, Gogotsi Y, Winey KI. An in situ Raman spectroscopy study of stress transfer between carbon nanotubes and polymer. *Nanotechnology* 2009;20:335703 (7 pp.).
- [79] Li JL, Wang LJ, He T, Jiang W. Surface graphitization and mechanical properties of hot-pressed bulk carbon nanotubes compacted by spark plasma sintering. *Carbon* 2007;45(13):2636–42.
- [80] Yu MF, Lourie O, Dyer MJ, Moloni K, Kelly TF, Ruoff RS. Strength and breaking mechanism of multiwalled carbon nanotubes under tensile load. *Science* 2000;287:637–40.